Theory of ultrafast x-ray scattering by molecules in the gas phase

Theory of Ultrafast X-Ray Scattering by Molecules in the Gas Phase

Mats Simmermacher,[1] Andrés Moreno Carrascosa,[1] Niels E. Henriksen,[2] Klaus B. Møller,[2, a)] and Adam Kirrander[1, b)]
[1)]*EaStCHEM, School of Chemistry, University of Edinburgh, EH9 3FJ, Edinburgh, United Kingdom.*
[2)]*Department of Chemistry, Technical University of Denmark, 2800 Lyngby, Denmark.*

(Dated: 23 August 2019)

We recast existing theory of ultrafast time-resolved x-ray scattering by molecules in the gas phase based on first-order time-dependent perturbation theory and quantum electrodynamics into a unified and coherent theoretical framework. The effect of the detection window is analyzed in detail and the contributions to the total scattering signal are discussed. This includes the coherent mixed component caused by interference between scattering amplitudes from different electronic states. A new detailed and fully converged simulation of ultrafast total x-ray scattering by excited H_2 molecules illustrates the theory and demonstrates that the inelastic component can contribute strongly, *i.e.* on the same order of magnitude as the elastic component, to the total difference scattering signal.

I. INTRODUCTION

A century after von Laue and the Braggs were awarded Nobel Prizes for x-ray diffraction from crystals[1], novel sources of x-rays permit experiments that their contemporaries could not have imagined. The new X-ray Free-Electron Lasers (XFELs) provide a peak brilliance more than 20 orders of magnitude greater than conventional x-ray tubes.[2–5] X-ray scattering is therefore no longer confined to crystalline samples where the scattering signal is enhanced by constructive interference from a periodic lattice and experiments in the gas or liquid phases are possible. Moreover, XFELs emit pulsed radiation that allows for investigation of structural changes and chemical reactions in real time.[6–18] In one remarkable example of these novel experiments, non-resonant scattering of hard x-rays from the Linac Coherent Light Source[2] was used to identify reaction paths of the electrocyclic ring-opening of 1,3-cyclohexadiene to 1,3,5-hexatriene[7,8], thus providing insights into chemical reaction mechanisms that are complementary to the information accessible from spectroscopy.[13,19] It is likely that the duration of pulses at XFELs will reduce further in the near future[20–24], making it possible to study even faster processes such as the rearrangement of electrons during chemical reactions.

In ultrafast x-ray scattering experiments a target molecule interacts with two sequential pulses of electromagnetic radiation, the pump and the probe. The pump pulse, normally generated by an optical laser, excites the molecule and thereby induces dynamics such as photochemical reactions or photophysical relaxation. The probe pulse, which has a mean photon energy in the hard x-ray regime of several keV, is scattered by the excited molecule onto a detector. By changing the pump-probe delay time, the scattering signal is measured at different points in time. The resulting series of snapshots contains time-resolved information about the dynamics triggered by the pump pulse.

Extracting information from the experimental data is non-trivial. Inversion procedures that transform the scattering signal directly into the electron density and thereby reveal the molecular structure rely on rough approximations such as the Independent Atom Model (IAM) and its underlying assumption that the time-dependent signal is elastic.[25–27] Inelastic scattering that involves a transfer of energy between the photons and the molecule is only accounted for in a very approximate manner, if at all. The validity of these approximations is not generally assured. The elastic and the inelastic signals are usually integrated on the detector and the inelastic contribution cannot generally be assumed to be constant.[28,29] The reorganization of the electron density due to bonding or electronic excitation is furthermore not accounted for in the framework of the IAM.[30,31] A particularly dramatic failure of the assumption that the time-dependent scattering signal is elastic was demonstrated in a seminal paper by Dixit, Vendrell, and Santra, who showed that the scattering signal of an electronic wave packet deviates substantially from the Fourier transform of the time-dependent electron density.[32] All of the above emphasizes that time-resolved scattering experiments must be accompanied by numerical simulations based on a sound and elaborate theoretical framework.

Pioneering work that addressed the theoretical description of time-resolved x-ray scattering was published by Wilson *et al.* already in the 1990s.[25,33,34] Without explicitly treating the x-ray pulse and its interaction with the material system in terms of electrodynamics, the authors extended the theory of conventional static scattering to the case of time-dependent states. Remarkably, their approach led to equations very similar to those obtained by more recent and fundamental derivations. Most notably, Cao and Wilson[25] could distinguish the same three components to the scattering signal identified in more recent work[28,35–37]: elastic scattering, inelastic scattering, and scattering related to electronic coherences.

In 2002, Bratos *et al.* discussed time-resolved x-ray scattering by incorporating the x-ray pulse in terms of classical electrodynamics.[38] Six years later, Henriksen and Møller provided a fully quantized description that utilized quantum electrodynamics[39], an approach they elaborated further in subsequent publications[26,27,40] and which was adapted for quantum molecular dynamics simulations by Kirrander *et al.*[41]. The already mentioned paper by Dixit *et al.* had provided the first simulation of time-resolved x-ray scattering that fully applied the quantum description to scattering by the

[a)]Electronic mail: kbmo@kemi.dtu.dk
[b)]Electronic mail: adam.kirrander@ed.ac.uk

hydrogen atom.[32] In 2017, Mukamel and co-workers calculated the x-ray scattering signal of sodium fluoride following UV excitation from the $X^1\Sigma^+$ ground state to the $A^1\Sigma^+$ excited state[35,37], showing that time-resolved x-ray scattering can carry signatures of short-lived electronic coherences created at the avoided crossing between the ground and excited state. Their treatment, however, considered only the two electronic states occupied by the wave packet, meaning that inelastic scattering to other bound states was neglected, and the scattering signal was reduced to a single dimension in reciprocal space. In a recent article[28], we addressed these aspects and investigated the role of electronic coherence further, reporting an extensive simulation of scattering from a wave packet in the hydrogen molecule.

Despite the advances made, it is clear that aspects of the theory of time-resolved x-ray scattering remain opaque, as exemplified by a recent debate regarding heterodyne interferences in the scattering signal of photoexcited molecules in the gas phase.[37,42–45] It is therefore necessary that the theory is discussed in greater detail and that the nature of the different contributions to the scattering signal are illustrated by simulations. With this in mind, we elaborate the theoretical framework for ultrafast scattering from molecules that was partially applied in our previous work[28], in particular with respect to different detection window limits and total scattering. The theory identifies the different components in the scattering signal and key aspects are explained in detail. As a concrete example of an application of the theory, a simulation of the total scattering signal of the hydrogen molecule subsequent to excitation from the $X^1\Sigma_g^+$ ground state to the $B^1\Sigma_u^+$ excited state and for an x-ray pulse with 10 fs duration is presented. All components of the total scattering signal are evaluated on a two-dimensional detector and their magnitudes are quantified and compared. This provides insights that extend our own previous work and the seminal contributions by Mukamel and co-workers and will hopefully contribute to a more complete understanding of time-resolved x-ray scattering by molecules.

II. THEORY

The time-resolved differential x-ray scattering signal $d\sigma/d\Omega$ per solid angle Ω obtained using first-order perturbation theory and a fully quantized description of the x-ray pulse is[39,40],

$$\frac{d\sigma}{d\Omega} = \left(\frac{d\sigma}{d\Omega}\right)_{\mathrm{Th}} \iiint \frac{\omega_\mathrm{s}}{\omega_0} I(t) C(\delta) e^{\imath(\omega_0-\omega_\mathrm{s})\delta} \times \mathfrak{L}(\boldsymbol{q},t,\delta)\, d\delta d\omega_\mathrm{s} dt, \tag{1}$$

where $(d\sigma/d\Omega)_{\mathrm{Th}}$ is the differential Thomson scattering cross-section for a free electron, $I(t)$ and $C(\delta)$ are the photon number intensity and the linear coherence function of the x-ray pulse with their corresponding times t and δ, and ω_0 and ω_s are the angular frequencies of the incident and scattered x-ray photons, respectively. $\mathfrak{L}(\boldsymbol{q},t,\delta)$ is the scattering probability at point $\boldsymbol{q}$ in reciprocal space at times t and δ. It is given by,

$$\mathfrak{L}(\boldsymbol{q},t,\delta) = \langle\Psi(t)|e^{\imath\hat{H}_M\delta/2\hbar}\hat{L}^\dagger e^{-\imath\hat{H}_M\delta/\hbar}\hat{L}e^{\imath\hat{H}_M\delta/2\hbar}|\Psi(t)\rangle, \tag{2}$$

where the bracket implies integration over all electronic $\bar{\boldsymbol{r}} = (\boldsymbol{r}_1,\ldots,\boldsymbol{r}_{N_\mathrm{e}})$ and nuclear $\bar{\boldsymbol{R}} = (\boldsymbol{R}_1,\ldots,\boldsymbol{R}_{N_\mathrm{at}})$ coordinates. Moreover, Eq. (2) contains the time-dependent wave function $|\Psi(t)\rangle$, the molecular Hamiltonian $\hat{H}_\mathrm{M}$, and the one-electron scattering operator $\hat{L} = \sum_{n=1}^{N_\mathrm{e}} \exp(\imath\boldsymbol{q}\cdot\boldsymbol{r}_n)$, where $\imath$ is the imaginary unit, $\hbar = h/2\pi$ Planck's constant, and $\boldsymbol{q} = \boldsymbol{k}_0 - \boldsymbol{k}_\mathrm{s}$ the scattering vector in terms of the wave vectors of the incident and the scattered photons, $\boldsymbol{k}_0$ and $\boldsymbol{k}_\mathrm{s}$. The sum runs over all N_e electrons of the molecule and $\boldsymbol{r}_n$ is the real-space coordinate of an electron with index n. We note that the pump-probe delay time is contained within $I(t)$ and that the effect of the pump pulse is embedded in the propagation of the molecular wave function $|\Psi(t)\rangle$.

The molecular wave function $|\Psi(t)\rangle$ in Eq. (2) can be expanded in a basis of N electronic eigenstates $|\varphi_k(\bar{\boldsymbol{R}})\rangle$ that depend parametrically on the coordinates $\bar{\boldsymbol{R}}$ of the N_at nuclei and obey the electronic Schrödinger equation $\hat{H}_\mathrm{e}\,|\varphi_k(\bar{\boldsymbol{R}})\rangle = V_k(\bar{\boldsymbol{R}})\,|\varphi_k(\bar{\boldsymbol{R}})\rangle$ with eigenvalues $V_k(\bar{\boldsymbol{R}})$,

$$|\Psi(t)\rangle = \sum_{k=1}^{N} |\chi_k(t)\rangle\,|\varphi_k(\bar{\boldsymbol{R}})\rangle, \tag{3}$$

where the time-dependent ket $|\chi_k(t)\rangle$ is the nuclear wave packet on electronic state k. It can be expressed as a time-dependent superposition of rovibrational eigenstates of the nuclear Schrödinger equation in the framework of the Born-Oppenheimer approximation, $\big(\hat{T}_\mathrm{N} + V_k(\bar{\boldsymbol{R}})\big)|\chi_{\bar{k}}\rangle = E_{\bar{k}}|\chi_{\bar{k}}\rangle$ with $\bar{k} = \{k, v_k, J_k\}$, where v_k and J_k are the vibrational and rotational quantum numbers, $\hat{T}_\mathrm{N}$ is the kinetic energy operator of the nuclei, and $E_{\bar{k}}$ is the total energy of the molecule in electronic state $|\varphi_k(\bar{\boldsymbol{R}})\rangle$. With time-dependent coefficients $a_{\bar{k}}(t)$, the superposition is,

$$|\chi_k(t)\rangle = \sum_{v_k}\sum_{J_k} a_{\bar{k}}(t)\,|\chi_{\bar{k}}\rangle. \tag{4}$$

Insertion of the resolution of the identity in the direct product basis of nuclear and electronic eigenstates,

$$\hat{\mathbf{1}} = \sum_{\bar{k}}^{\infty} |\varphi_k(\bar{\boldsymbol{R}})\rangle|\chi_{\bar{k}}\rangle\langle\chi_{\bar{k}}|\langle\varphi_k(\bar{\boldsymbol{R}})|, \tag{5}$$

after each of the three exponential time-propagation operators in Eq. (2), yields the scattering probability in terms of,

$$\mathfrak{L}(\boldsymbol{q},t,\delta) = \sum_{i,j}^{N}\sum_{v_i,J_i}^{\infty}\sum_{v_j,J_j}^{\infty}\sum_{\bar{f}}^{\infty} e^{-\imath\omega_{\bar{f}\bar{i}\bar{j}}\delta} a^*_{\bar{f}}(t)a_{\bar{i}}(t) \times \langle\chi_{\bar{j}}|\,L^*_{fj}(\boldsymbol{q},\bar{\boldsymbol{R}})\,|\chi_{\bar{f}}\rangle\,\langle\chi_{\bar{f}}|\,L_{fi}(\boldsymbol{q},\bar{\boldsymbol{R}})\,|\chi_{\bar{i}}\rangle, \tag{6}$$

where $\omega_{\bar{f}\bar{i}\bar{j}} = \big(E_{\bar{f}} - [E_{\bar{i}} + E_{\bar{j}}]/2\big)/\hbar$ and the action of the molecular Hamiltonian upon the nuclear and electronic eigenstates is approximated adiabatically as,

$$e^{-\frac{\imath}{\hbar}\hat{H}_\mathrm{M}\delta}\,|\varphi_k(\bar{\boldsymbol{R}})\rangle|\chi_{\bar{k}}\rangle \approx e^{-\frac{\imath}{\hbar}E_{\bar{k}}\delta}\,|\varphi_k(\bar{\boldsymbol{R}})\rangle|\chi_{\bar{k}}\rangle. \tag{7}$$

We note that Eq. (7) is applied to the propagation in time δ only and does not imply that the molecular wave packet itself evolves adiabatically. The wave packet is propagated in time t and non-adiabatic effects can thus be accounted for fully (*see also footnote*[46]).

The scattering probability $\mathfrak{L}(\boldsymbol{q},t,\delta)$ in Eq. (6) contains scattering amplitudes given by one-electron scattering matrix elements,

$$L_{fi}(\boldsymbol{q},\bar{\boldsymbol{R}}) = \langle\varphi_f(\bar{\boldsymbol{R}})|\hat{L}|\varphi_i(\bar{\boldsymbol{R}})\rangle = \langle\varphi_i(\bar{\boldsymbol{R}})|\hat{L}^\dagger|\varphi_f(\bar{\boldsymbol{R}})\rangle^*, \quad (8)$$

which are Fourier transformed expectation values of the one-electron density operator, $\hat{\rho}(\boldsymbol{r}) = \sum_{n=1}^{N_\mathrm{e}} \delta(\boldsymbol{r}-\boldsymbol{r}_n)$,[47] where the sum runs over all electronic coordinates of the molecule and $\delta(\boldsymbol{r}-\boldsymbol{r}_n)$ is a Dirac delta function that sifts out the electronic coordinate $\boldsymbol{r}_n$. The Fourier transform from real to reciprocal space is,

$$L_{fi}(\boldsymbol{q},\bar{\boldsymbol{R}}) = \int_{-\infty}^{+\infty} e^{\imath\boldsymbol{q}\cdot\boldsymbol{r}}\rho_{fi}(\boldsymbol{r},\bar{\boldsymbol{R}})\, d\boldsymbol{r}, \quad (9)$$

with

$$\rho_{fi}(\boldsymbol{r},\bar{\boldsymbol{R}}) = \langle\varphi_f(\bar{\boldsymbol{R}})|\hat{\rho}(\boldsymbol{r})|\varphi_i(\bar{\boldsymbol{R}})\rangle, \quad (10)$$

which for $f=i$ is the one-electron density (often just called the electron density) and for $f\neq i$ is the one-electron transition density.

Using the scattering probability from Eq. (6), the x-ray scattering signal given by Eq. (1) becomes[40],

$$\begin{aligned}\frac{d\sigma}{d\Omega} = \left(\frac{d\sigma}{d\Omega}\right)_{\mathrm{Th}} \sum_{i,j}^{N}\sum_{\nu_i,J_i}^{\infty}\sum_{\nu_j,J_j}^{\infty}\sum_{\bar{f}}^{\infty}\iiint \frac{\omega_\mathrm{s}}{\omega_0} I(t)\, a_{\bar{j}}^*(t)\, a_{\bar{i}}(t) \\ \times C(\delta)\, e^{-\imath(\omega_\mathrm{s}-\omega_0+\omega_{\bar{f}\bar{i}\bar{j}})\delta}\, \langle\chi_{\bar{j}}|\, L_{fj}^*(\boldsymbol{q},\bar{\boldsymbol{R}})\, |\chi_{\bar{f}}\rangle \\ \times \langle\chi_{\bar{f}}|\, L_{fi}(\boldsymbol{q},\bar{\boldsymbol{R}})\, |\chi_{\bar{i}}\rangle\, d\delta d\omega_\mathrm{s} dt.\end{aligned} \quad (11)$$

The integral over δ in Eq. (11) is a Fourier transform of the linear coherence function $C(\delta)$ and equal to the spectral density at angular frequencies $\omega_\mathrm{s}-\omega_0+\omega_{\bar{f}\bar{i}\bar{j}}$,

$$F\left(\omega_\mathrm{s}-\omega_0+\omega_{\bar{f}\bar{i}\bar{j}}\right) = \int_{-\infty}^{+\infty} C(\delta)\, e^{-\imath(\omega_\mathrm{s}-\omega_0+\omega_{\bar{f}\bar{i}\bar{j}})\delta}\, d\delta. \quad (12)$$

Hence, Eq. (11) can be re-written as,

$$\begin{aligned}\frac{d\sigma}{d\Omega} = \left(\frac{d\sigma}{d\Omega}\right)_{\mathrm{Th}} \sum_{i,j}^{N}\sum_{\nu_i,J_i}^{\infty}\sum_{\nu_j,J_j}^{\infty}\sum_{\bar{f}}^{\infty}\iint \frac{\omega_\mathrm{s}}{\omega_0} I(t)\, a_{\bar{j}}^*(t)\, a_{\bar{i}}(t) \\ \times F\left(\omega_\mathrm{s}-\omega_0+\omega_{\bar{f}\bar{i}\bar{j}}\right)\, \langle\chi_{\bar{j}}|\, L_{fj}^*(\boldsymbol{q},\bar{\boldsymbol{R}})\, |\chi_{\bar{f}}\rangle \\ \times \langle\chi_{\bar{f}}|\, L_{fi}(\boldsymbol{q},\bar{\boldsymbol{R}})\, |\chi_{\bar{i}}\rangle\, d\omega_\mathrm{s} dt,\end{aligned} \quad (13)$$

Following the common approximation first introduced by Waller and Hartree[48], we can further assume that the difference in energy between the incident and scattered photon is small compared to the mean photon energy of the x-ray pulse, *i.e.* $\omega_\mathrm{s}\approx\omega_0$. Thus, the scattering vector $\boldsymbol{q}$ that generally depends on both ω_0 and ω_s becomes independent of ω_s and Eq. (13) simplifies to,

$$\begin{aligned}\frac{d\sigma}{d\Omega} = \left(\frac{d\sigma}{d\Omega}\right)_{\mathrm{Th}} \sum_{i,j}^{N}\sum_{\nu_i,J_i}^{\infty}\sum_{\nu_j,J_j}^{\infty}\sum_{\bar{f}}^{\infty} W_{\bar{f}\bar{i}\bar{j}}(\Delta\omega) \\ \times \langle\chi_{\bar{j}}|\, L_{fj}^*(\tilde{\boldsymbol{q}},\bar{\boldsymbol{R}})\, |\chi_{\bar{f}}\rangle\, \langle\chi_{\bar{f}}|\, L_{fi}(\tilde{\boldsymbol{q}},\bar{\boldsymbol{R}})\, |\chi_{\bar{i}}\rangle \\ \times \int I(t)\, a_{\bar{j}}^*(t)\, a_{\bar{i}}(t)\, dt,\end{aligned} \quad (14)$$

where $\tilde{\boldsymbol{q}}$ denotes a scattering vector that does not depend on ω_s and $W_{\bar{f}\bar{i}\bar{j}}(\Delta\omega)$ refers to the remaining integral over ω_s which acts as a window function,

$$W_{\bar{f}\bar{i}\bar{j}}(\Delta\omega) = \int_{\omega_0-\Delta\omega}^{\omega_0+\Delta\omega} F\left(\omega_\mathrm{s}-\omega_0+\omega_{\bar{f}\bar{i}\bar{j}}\right)\, d\omega_\mathrm{s}. \quad (15)$$

The parameter $\Delta\omega$ in Eq. (15) defines the detection window, *i.e.* the range of angular frequencies around the mean ω_0 that are accepted by the detector. The parameter $\Delta\omega$ has to be significantly smaller than ω_0 to ensure that the assumption $\omega_\mathrm{s}\approx\omega_0$ is justified.

In the following, two different detection window limits as well as their implications are discussed. We note that a similar analysis of the effects of the window function was published earlier by Dixit, Slowik, and Santra.[49]

A. Intermediate Detection Window

Considering that mean photon energies of several keV are used in non-resonant x-ray scattering experiments, the detection window $\Delta\omega$ can be much larger than the rovibrational transition energies of the molecule. Under such conditions, inelastic transitions to all nuclear eigenstates are detected with equal weight and the window function becomes independent of the rovibrational quantum numbers,

$$W_{\bar{f}\bar{i}\bar{j}}(\Delta\omega) \approx W_{fij}(\Delta\omega), \quad (16)$$

where $W_{fij}(\Delta\omega)$ depends only on the electronic energies. Eq. (16) implies that $\omega_{\bar{f}\bar{i}\bar{j}}$ involved in Eq. (15) can be replaced by an angular frequency $\omega_{fij} = \left(V_f - [V_i+V_j]/2\right)/\hbar$ with V_f the electronic energy of electronic state $|\varphi_f(\bar{\boldsymbol{R}})\rangle$. Since Eq. (16) requires that differences on the order of the rovibrational energies do not alter the window function, the precise value of the electronic energies is not very important and a sensible choice is $V_f = V_f(\bar{\boldsymbol{R}}_0)$, where $\bar{\boldsymbol{R}}_0$ is the equilibrium geometry. Note that Eq. (16) retroactively justifies the adiabatic approximation made in Eq. (7). The non-adiabatic couplings of the electronic and nuclear motion can be neglected when the propagation in time δ is considered, since the choice of the detection window $\Delta\omega$ implies that the detector is not sensitive to the resulting changes in photon energy.

Within the limit of the approximation embodied by Eq. (16), the differential scattering signal in Eq. (14) simplifies to,

$$\begin{aligned}\frac{d\sigma}{d\Omega} = \left(\frac{d\sigma}{d\Omega}\right)_{\mathrm{Th}} \sum_{i,j}^{N}\sum_{f}^{\infty} W_{fij}(\Delta\omega) \int I(t) \\ \times \langle\chi_j(t)|\, L_{fj}^*(\tilde{\boldsymbol{q}},\bar{\boldsymbol{R}}) L_{fi}(\tilde{\boldsymbol{q}},\bar{\boldsymbol{R}})\, |\chi_i(t)\rangle\, dt,\end{aligned} \quad (17)$$

where the three sums over the rovibrational eigenstates have been eliminated using Eq. (4) and the resolution of the identity in the nuclear subspace, $\hat{\mathbf{1}}_{\bar{\boldsymbol{R}}} = \sum_{v_k,J_k}^{\infty} |\chi_{\bar{k}}\rangle\langle\chi_{\bar{k}}|$. Eq. (17) permits the identification of three different components in the scattering signal,

$$\frac{d\sigma}{d\Omega} = \frac{d\sigma_{\mathrm{e}}}{d\Omega} + \frac{d\sigma_{\mathrm{i}}}{d\Omega} + \frac{d\sigma_{\mathrm{cm}}}{d\Omega}. \tag{18}$$

First, if all indices are the same, *i.e.* if $i = j = f$, the scattering signal will be *elastic*,

$$\frac{d\sigma_{\mathrm{e}}}{d\Omega} = \left(\frac{d\sigma}{d\Omega}\right)_{\mathrm{Th}} W(\Delta\omega) \sum_{i}^{N} \int I(t) \times \langle\chi_i(t)| \, |L_{ii}(\tilde{\boldsymbol{q}},\bar{\boldsymbol{R}})|^2 \, |\chi_i(t)\rangle \, dt, \tag{19}$$

where the window function $W(\Delta\omega)$ is independent of the electronic state indices, since $\omega_{fij} = 0$. Second, if $i = j \neq f$, the scattering signal will be *electronically inelastic*,

$$\frac{d\sigma_{\mathrm{i}}}{d\Omega} = \left(\frac{d\sigma}{d\Omega}\right)_{\mathrm{Th}} \sum_{i}^{N} \sum_{f\neq i}^{\infty} W_{fi}(\Delta\omega) \int I(t) \times \langle\chi_i(t)| \, |L_{fi}(\tilde{\boldsymbol{q}},\bar{\boldsymbol{R}})|^2 \, |\chi_i(t)\rangle \, dt, \tag{20}$$

where $W_{fi}(\Delta\omega)$ depends on the angular frequency of the inelastic transition, $\omega_{fi} = (V_f - V_i)/\hbar$. Third, if $i \neq j$, the scattering signal will be what we call *coherent mixed*,

$$\frac{d\sigma_{\mathrm{cm}}}{d\Omega} = 2\left(\frac{d\sigma}{d\Omega}\right)_{\mathrm{Th}} \sum_{i}^{N-1} \sum_{j>i}^{N} \sum_{f}^{\infty} W_{fij}(\Delta\omega) \int I(t) \times \mathrm{Re}\left[\langle\chi_j(t)| \, L^*_{fj}(\tilde{\boldsymbol{q}},\bar{\boldsymbol{R}}) L_{fi}(\tilde{\boldsymbol{q}},\bar{\boldsymbol{R}}) \, |\chi_i(t)\rangle\right] \, dt. \tag{21}$$

The coherent mixed component in Eq. (21) is caused by intramolecular interference of scattering amplitudes from different electronic states, $|\varphi_i(\bar{\boldsymbol{R}})\rangle$ and $|\varphi_j(\bar{\boldsymbol{R}})\rangle$, that have nonzero population in the molecular wave packet given by Eq. (3). The product of one-electron scattering matrix elements in Eq. (21) is weighted by the product of the corresponding nuclear wave packets, $|\chi_i(t)\rangle$ and $|\chi_j(t)\rangle$, on each of the superposed electronic states. The coherent mixed component is therefore a direct probe of the degree of transient electronic coherence or wave packet overlap, respectively.[28,35,37] In systems that become decoherent within a few femtoseconds[50,51], the component will vanish accordingly. Moreover, the coherent mixed scattering displays a rapid beating with a period of $T = h/\Delta V_{ij}$, where ΔV_{ij} is the difference in energy of the two superposed states at the time when the coherence is created. The coherent mixed component will only be resolved if the duration of the x-ray probe pulse described by $I(t)$ is shorter than this period.

B. Large Detection Window

A mean photon energy of several keV also permits a detection window $\Delta\omega$ that is much larger than the electronic transition energies of the molecule without invalidating the approximation $\omega_{\mathrm{s}} \approx \omega_0$. Under such conditions, inelastic transitions to all electronic eigenstates are detected with equal weight and the window function becomes generally independent of the angular frequency ω_{fij},

$$W_{fij}(\Delta\omega) \approx W(\Delta\omega). \tag{22}$$

When Eq. (22) is valid, the differential scattering signal in Eq. (17) simplifies further to,

$$\frac{d\sigma}{d\Omega} = \left(\frac{d\sigma}{d\Omega}\right)_{\mathrm{Th}} W(\Delta\omega) \times \sum_{i,j}^{N} \int I(t) \, \langle\chi_j(t)| \, \Lambda_{ji}(\tilde{\boldsymbol{q}},\bar{\boldsymbol{R}}) \, |\chi_i(t)\rangle \, dt, \tag{23}$$

where the infinite sum over the electronic eigenstates has been eliminated by recognizing the resolution of the identity in the electronic subspace, $\hat{\mathbf{1}}_{\bar{\boldsymbol{r}}} = \sum_f^{\infty} |\varphi_f(\bar{\boldsymbol{R}})\rangle\langle\varphi_f(\bar{\boldsymbol{R}})|$. Eq. (23) contains two-electron scattering matrix elements,

$$\begin{aligned}\Lambda_{ji}(\tilde{\boldsymbol{q}},\bar{\boldsymbol{R}}) &= \langle\varphi_j(\bar{\boldsymbol{R}})| \, \hat{\tilde{L}}^{\dagger}\hat{\tilde{L}} \, |\varphi_i(\bar{\boldsymbol{R}})\rangle \\ &= \sum_{m,n}^{N_{\mathrm{e}}} \langle\varphi_j(\boldsymbol{r})|e^{\imath\tilde{\boldsymbol{q}}\cdot(\boldsymbol{r}_n - \boldsymbol{r}_m)}|\varphi_i(\boldsymbol{r})\rangle,\end{aligned} \tag{24}$$

where $\hat{\tilde{L}}$ is the one-electron scattering operator that depends on $\tilde{\boldsymbol{q}}$. Since terms with $m = n$ in Eq. (24) reduce to the Kronecker delta δ_{ij}, the two-electron scattering matrix element can be written as,

$$\Lambda_{ji}(\tilde{\boldsymbol{q}},\bar{\boldsymbol{R}}) = N_{\mathrm{e}} \, \delta_{ij} + \Lambda'_{ji}(\tilde{\boldsymbol{q}},\bar{\boldsymbol{R}}), \tag{25}$$

where $\Lambda'_{ji}(\tilde{\boldsymbol{q}},\bar{\boldsymbol{R}})$ is the pure two-electron part of $\Lambda_{ji}(\tilde{\boldsymbol{q}},\bar{\boldsymbol{R}})$ with $m \neq n$. Similarly to how the one-electron scattering matrix element $L_{fi}(\boldsymbol{q},\bar{\boldsymbol{R}})$ is related to the Fourier transformed expectation value of the one-electron density operator by Eqs. (9–10), $\Lambda'_{ji}(\tilde{\boldsymbol{q}},\bar{\boldsymbol{R}})$ is a doubly Fourier transformed expectation value of the two-electron density operator, $\hat{\rho}(\boldsymbol{r}_1,\boldsymbol{r}_2) = (1/2) \, \sum_m^N \sum_{n\neq m}^N \, \delta(\boldsymbol{r}_1 - \boldsymbol{r}_m)\delta(\boldsymbol{r}_2 - \boldsymbol{r}_n)$,[47]

$$\Lambda'_{ji}(\tilde{\boldsymbol{q}},\bar{\boldsymbol{R}}) = 2\iint_{-\infty}^{+\infty} e^{\imath\tilde{\boldsymbol{q}}\cdot(\boldsymbol{r}_2 - \boldsymbol{r}_1)} \, \rho_{ji}(\boldsymbol{r}_1,\boldsymbol{r}_2,\bar{\boldsymbol{R}}) \, d\boldsymbol{r}_1 d\boldsymbol{r}_2, \tag{26}$$

where

$$\rho_{ji}(\boldsymbol{r}_1,\boldsymbol{r}_2,\bar{\boldsymbol{R}}) = \langle\varphi_j(\bar{\boldsymbol{R}})|\hat{\rho}(\boldsymbol{r}_1,\boldsymbol{r}_2)|\varphi_i(\bar{\boldsymbol{R}})\rangle. \tag{27}$$

Analogous to Eq. (18) in the limit of the intermediate detection window, three distinct components of the scattering can be identified in Eq. (23),

$$\frac{d\sigma}{d\Omega} = \frac{d\sigma_{\mathrm{bg}}}{d\Omega} + \frac{d\sigma_{2\mathrm{e}}}{d\Omega} + \frac{d\sigma_{\mathrm{cm}}}{d\Omega}. \tag{28}$$

The first contribution to Eq. (28) forms a constant *background*,

$$\frac{d\sigma_{\mathrm{bg}}}{d\Omega} = \left(\frac{d\sigma}{d\Omega}\right)_{\mathrm{Th}} N_{\mathrm{e}} \, W(\Delta\omega) \, I, \tag{29}$$

where $I = \int I(t) \, dt$ is the integrated photon number intensity of the x-ray pulse. This contribution originates from the

first term of the two-electron scattering matrix element in Eq. (25), $N_e\ \delta_{ij}$, and corresponds to the scattering signal from N_e free electrons. It reflects that from the perspective of an x-ray photon an electron can move freely within the bound system when all electronic transitions are allowed with equal weight. Thus, $d\sigma_{bg}/d\Omega$ is a global, time-independent quantity that can be subtracted from the total scattering signal without loss of structural information. It is the *one-electron part* of the sum of the elastic and inelastic components, Eqs. (19) and (20), in the limit of a detection window that is much larger than the electronic transition energies of the molecule.

The second contribution to Eq. (28) is the *two-electron* component,

$$\frac{d\sigma_{2e}}{d\Omega} = \left(\frac{d\sigma}{d\Omega}\right)_{Th} W(\Delta\omega) \times \sum_i^N \int I(t)\ \langle\chi_i(t)|\ \Lambda'_{ii}(\tilde{\boldsymbol{q}},\bar{\boldsymbol{R}})\ |\chi_i(t)\rangle\ dt, \tag{30}$$

which originates from the two-electron scattering matrix element in Eq. (25), $\Lambda'_{ji}(\tilde{\boldsymbol{q}},\bar{\boldsymbol{R}})$, with $i=j$. As its name suggests, it is the pure *two-electron part* of the sum of the elastic and inelastic components in the limit of a large detection window. It corresponds to what Waller and Hartree have termed *excess scattering*.[48] Since the one-electron part in Eq. (29) forms a constant background, all structural information in Eq. (23) is contained in $d\sigma_{2e}/d\Omega$. This shows, together with Eq. (26), that total scattering by molecules in the gas phase measures more than just the one-electron density, in marked contrast to diffraction from crystalline matter which is predominantly elastic and probes almost selectively the one-electron density.

Finally, the third contribution to Eq. (28) corresponds to the previously discussed *coherent mixed* component,

$$\frac{d\sigma_{cm}}{d\Omega} = 2\left(\frac{d\sigma}{d\Omega}\right)_{Th} W(\Delta\omega) \sum_i^{N-1}\sum_{j>i}^{N} \times \mathrm{Re}\left[\int I(t)\ \langle\chi_j(t)|\ \Lambda'_{ji}(\tilde{\boldsymbol{q}},\bar{\boldsymbol{R}})\ |\chi_i(t)\rangle\ dt\right], \tag{31}$$

which stems from the element $\Lambda'_{ji}(\tilde{\boldsymbol{q}},\bar{\boldsymbol{R}})$ with $i\neq j$ and is the coherent mixed component from Eq. (21) in the limit of a large detection window. Note that this component will vanish if the two electronic states, $|\varphi_i(\bar{\boldsymbol{R}})\rangle$ and $|\varphi_j(\bar{\boldsymbol{R}})\rangle$, have different inversion symmetry, *i.e.* if one state is *gerade* and the other *ungerade*. This follows from the symmetry properties of the two-electron scattering matrix element $\Lambda'_{ji}(\tilde{\boldsymbol{q}},\bar{\boldsymbol{R}})$.[40]

Comparing the intermediate and large detection window limits, the main difference between the coherent mixed components with $i\neq j$ is that the sum for the large window runs over the occupied electronic states only, since the transitions to all final states $|\varphi_f(\bar{\boldsymbol{R}})\rangle$ are accounted for implicitly. With $i=j$, the elastic and inelastic components map onto the background and two-electron components. This is analogous to how the elastic and inelastic components add up to the *total scattering*[29] in the situation where the coherent mixed component vanishes due to either insufficient electronic coherence, an incoherent x-ray pulse, or a lack of time-resolution.

III. SIMULATION

To illustrate the theory discussed in Section II, we present a simulation of the ultrafast total x-ray scattering signal in the limit of a large detection window by the hydrogen molecule in a non-stationary state. This includes an analysis of the elastic and inelastic components.

Initially, the molecule is in the electronic and vibrational ground state $X^1\Sigma_g^+(v=0)$. It is excited by a transform-limited Gaussian extreme ultraviolet (XUV) pulse centred at $t=0$ fs, that has a full-width half-maximum (FWHM) duration of 25 fs and a mean photon energy of 14.3 eV. The electric field amplitude of the pump pulse is 53.8 MV/cm, which corresponds to a peak intensity of 7.69 TW/cm^2. The pump excites 10% of the population to the first excited electronic state, $B^1\Sigma_u^+ \leftarrow X^1\Sigma_g^+(v=0)$. Two other transitions that are accessible in principle, $C^1\Pi_u \leftarrow X^1\Sigma_g^+(v=0)$ and $B'^1\Sigma_u^+ \leftarrow X^1\Sigma_g^+(v=0)$, are not included for the sake of simplicity. The same parameters were applied in a previous study[28] and a similar wave packet has been probed experimentally by strong-field dissociative ionization[52].

The two-dimensional differential scattering signal $d\sigma/d\Omega$ is simulated for coherent and transform-limited x-ray pulses with a photon number intensity described by a normalized Gaussian function,

$$I(t) = \frac{1}{\sigma\sqrt{2\pi}} e^{-\frac{(t-\tau)^2}{2\sigma^2}}, \tag{32}$$

where τ is the pump-probe delay time and the pulse has a duration of $d_x = 10$ fs (FWHM), which corresponds to a standard deviation of $\sigma = d_x/(2\sqrt{2\ln 2})$. The mean photon energy of the pulse is $\hbar\omega_0 = 8.5$ keV. It propagates in laboratory $\hat{z}$ direction, while the H–H bond of the hydrogen molecule is assumed to be perfectly aligned with the laboratory $\hat{x}$ axis. Rotational wave packets are not considered. In accordance with the limit of a large detection window defined by Eq. (22), it is assumed that all inelastic transitions within the molecule are contributing with equal weight, *i.e.* $W(\Delta\omega)\approx 1$. The detection window and the chosen pulse duration preclude a detection of the coherent mixed component and the total signal is therefore elastic and inelastic only.

A. Computational Details

The simulations include the first two electronic singlet states of the hydrogen molecule, $X^1\Sigma_g^+$ and $B^1\Sigma_u^+$. They are calculated using state-average complete active space self-consistent field SA-CASSCF(2,20)[53]/d-aug-cc-pVQZ[54] in the *ab-initio* software package MOLPRO[55]. The active space contains the 20 energetically lowest-lying molecular orbitals. The two states are computed for H–H bond lengths in the range of $0.500\ \text{Å} \le R \le 6.500\ \text{Å}$ in steps of $\Delta R = 0.025$ Å. The molecular orbital coefficients and CI vectors are optimized to convergence thresholds of 10^{-6} and stored for later use when larger than 5×10^{-5}. Similarly, the one- and two-electron density matrices in the basis of natural orbitals are

calculated and stored.

From these two electronic states, all diagonal one- and two-electron scattering matrix elements are computed using our own scattering codes[30,56,57]. The evaluation of the two-electron scattering matrix elements is based on the work of Wang and Smith[58], but does not involve the spherical average. Each of the resulting 964 matrix elements is evaluated on a two-dimensional grid in the q_x-q_y plane that comprised 1210 points distributed across 19 equally spaced concentric circles with one point at the origin. The scattering matrix elements are interpolated to a smaller grid spacing of $\Delta R = 0.005$ Å to match the quantum dynamics simulation (*see below*).

The nuclear wave packet is propagated with the split-operator method[59] implemented in the WavePacket program[60]. The initial wave packet is the vibrational ground state, $X\,^1\Sigma_g^+(v=0)$, calculated with the Fourier DVR method[61]. The wave packet is propagated from $t = -100.00$ fs to $t = 350.00$ fs in time steps of $\Delta t = 0.01$ fs and the pump pulse described above is included explicitly in the simulations. The dynamics on the potential energy curve of the $B\,^1\Sigma_u^+$ state is adiabatic, since the non-adiabatic coupling[62] to the $B'\,^1\Sigma_u^+$ state is insufficient to lead to non-adiabatic population transfer. The simulation was run on a regular spatial grid with H–H bond lengths of $0.500\ \text{Å} \leq R \leq 6.500\ \text{Å}$ with steps of $\Delta R = 0.005$ Å. The highly accurate benchmark potential energy curves[63,64] and transition dipole moments[65] of Wolniewicz *et al.* are used in the simulations.

With the electronic energies, the one- and two-electron scattering matrix elements, and the nuclear wave packets at hand, the total differential x-ray scattering signal and its elastic components are calculated by means of Eqs. (28) to (31) and (19), respectively. The inelastic component is obtained by subtraction of the elastic from the total signal. The integrals over t and R are evaluated numerically by the trapezoidal rule. Difference scattering signals are obtained by subtraction of the stationary ground state reference signal at $\tau = -100$ fs (*i.e.* pump on − pump off).

B. Results

The two calculated potential energy curves $V_k(R)$ of the $X\,^1\Sigma_g^+$ and the $B\,^1\Sigma_u^+$ states of the hydrogen molecule are shown in Fig. 1. The curves are in close agreement with the highly accurate benchmark data from Wolniewicz *et al.* [63,64]. They deviate by 48 meV and 49 meV at most and by 11 meV and 30 meV on average, respectively. Considering furthermore that additional MRCI[66–68] calculations performed at a few representative values of R lead only to an insignificantly better agreement, one can conclude that results are close to the full-CI limit for the chosen basis set.

The nuclear density propagated on the adiabatic potential energy curve of the excited $B\,^1\Sigma_u^+$ state, $|\chi_B(R,t)|^2$, is shown in Fig. 2. At around $t \approx 0$ fs and $R \approx 0.76$ Å, a Franck-Condon wave packet is excited from the ground state. Because the potential energy curve of $B\,^1\Sigma_u^+$ has a negative gradient at that point, the wave packet accelerates towards larger

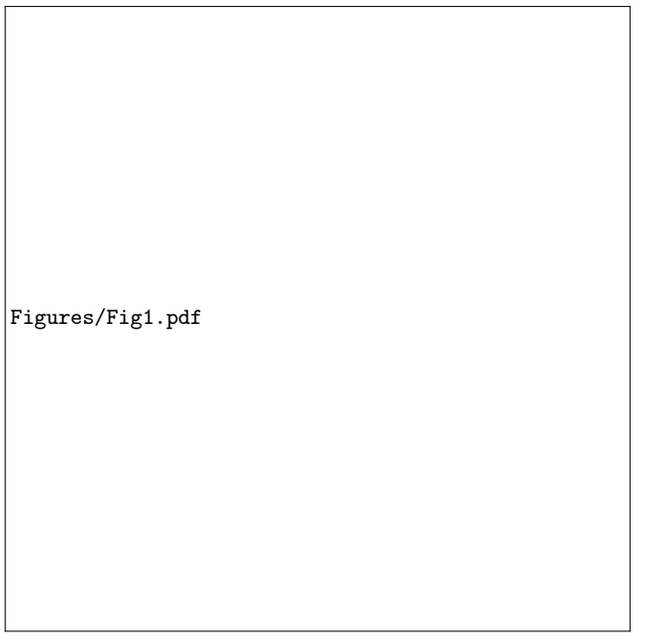

FIG. 1. Adiabatic potential energy curves $V_k(R)$ of the nine energetically lowest-lying electronic singlet states of the hydrogen molecule at different H–H bond lengths R. The $X\,^1\Sigma_g^+$ and $B\,^1\Sigma_u^+$ states are calculated with state-average CASSCF(2,20)/d-aug-cc-pVQZ and are visually indistinguishable from the highly accurate benchmark data of Wolniewicz *et al.*[63,64]. All energetically higher-lying states are shown for orientation and are taken from of Wolniewicz *et al.*[64,69–71]. The two states $C\,^1\Pi_u$ and $I\,^1\Pi_g$ are each doubly degenerate.

H–H bond lengths R. At $t \approx 31$ fs, the wave packet reaches the outer turning point with a maximum mean bond length of $\langle R \rangle \approx 5.18$ Å. The wave packet then accelerates towards smaller R and reaches the inner turning point with a minimum mean bond length of $\langle R \rangle \approx 2.33$ Å at $t \approx 62$ fs. After that, the wave packet continues to oscillate between the inner and outer turning points with a period of $T_{vib} \approx 62$ fs. The mean bond length $\langle R \rangle$ at the inner and outer turning points is slightly increasing and decreasing over time, respectively, reflecting the gradual dispersion of the wave packet. Moreover, the nodal structure in the density that becomes visible after the first outer turning point reflects that the wave packet is vibrationally highly excited. The XUV pump pulse has enough energy to excite vibrational eigenstates up to $B\,^1\Sigma_u^+(v=28)$. The nuclear wave packet on $X\,^1\Sigma_g^+$, in contrast, remains essentially stationary with its population depleted by 10%.

Following Eqs. (19) and (30), the evolution of the nuclear densities $|\chi_X(R,t)|^2$ and $|\chi_B(R,t)|^2$ determine the time-dependent changes in the elastic and inelastic components of the total scattering signal. Detector images of the resulting total difference scattering patterns (pump on − pump off) as well as their elastic and inelastic components are shown in Fig. 3 for three representative pump-probe delay times τ that cover a full period of the nuclear oscillation. The scattering intensities are given in units of the Thomson scattering cross-section $(d\sigma/d\Omega)_{\text{Th}}$ throughout.

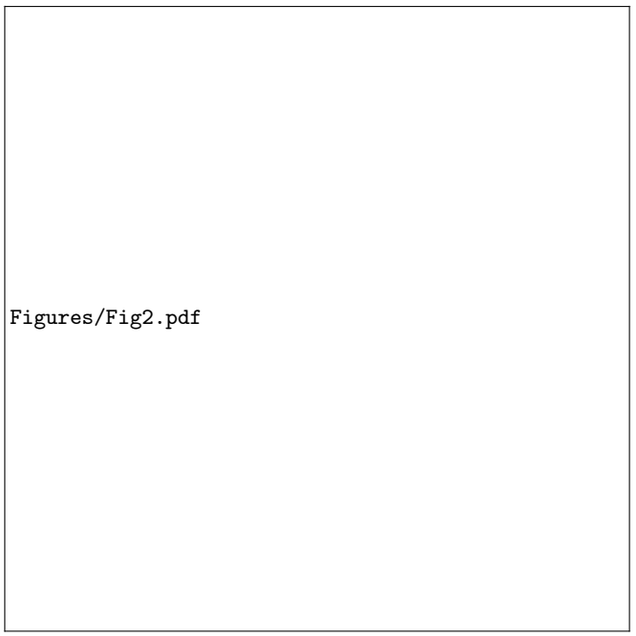

FIG. 2. Contour plot of the simulated nuclear density $|\chi_B(R,t)|^2$ on the $B\,^1\Sigma_u^+$ state of the hydrogen molecule at different H–H bond lengths R and times t. The nuclear wave packet $\chi_B(R,t)$ is prepared by XUV laser excitation from the $X\,^1\Sigma_g^+(v=0)$ ground state. The pump pulse is centred at $t=0$ fs and has a duration of 25 fs (FWHM), a mean photon energy of 14.3 eV, and a peak intensity of 7.69 TW/cm^2. The final population in the $B\,^1\Sigma_u^+$ state is 10%.

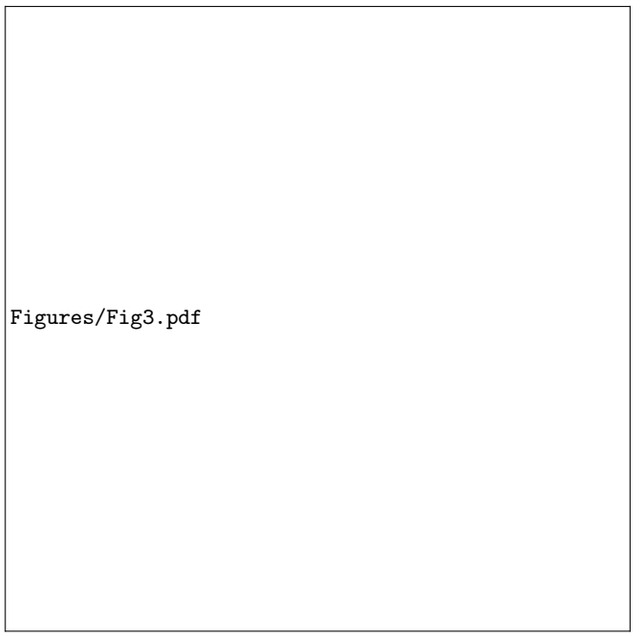

FIG. 3. Detector images of the time-resolved difference scattering patterns (pump on − pump off) for the elastic (top row) and inelastic (middle row) components of the total scattering signal (bottom row) simulated at three different pump-probe delay times τ. The delay times correspond to the outer, inner, and outer turning points (left to right) of the nuclear wave packet on the $B\,^1\Sigma_u^+$ state of the hydrogen molecule with a vibrational period of $T_{vib} \approx 62$ fs. The radial coordinate of the detector takes values of $0 \le q \le 4.31$ Å^{-1}. The patterns are calculated for an x-ray pulse duration of $d_x = 10$ fs (FWHM) and a mean photon energy of $\hbar\omega_0 = 8.5$ keV. The scattering intensity is given in units of the Thomson scattering cross-section, $(d\sigma/d\Omega)_{Th}$. The elastic patterns are practically identical to those calculated previously for a two orders of magnitude shorter x-ray pulse duration.[28]

The elastic difference scattering patterns in the top row of Fig. 3 are practically identical to those presented in our previous work[28], regardless that the x-ray pulse duration is two orders of magnitude longer. The patterns are negative everywhere in the detector plane at all pump-probe delay times τ. This reflects the fact that the one-electron density of the $B\,^1\Sigma_u^+$ state is more diffuse than the one-electron density of the ground state. In compliance with Friedel's law, the elastic patterns display a centrosymmetric D_2 rosette group symmetry. Each pattern has two symmetric minima on the horizontal q_x axis. At $\tau = T_{vib}$, when $\chi_B(R,t)$ reaches its inner turning point first, the minima take a value of roughly -0.26 at $q_x \approx \pm 0.93$ Å^{-1}. At $\tau = (1/2)\,T_{vib}$ and $\tau = (3/2)\,T_{vib}$, when $\chi_B(R,t)$ reaches its outer turning point for the first and second time, respectively, the minima decrease to -0.34 and move closer to the origin to $q_x \approx \pm 0.68$ Å^{-1}. These changes reveal that the one-electron density is shifted from the centre of the molecule towards its periphery, thereby adjusting to the increase of $\langle R \rangle$.

The inelastic difference scattering signals in the middle row of Fig. 3 are completely positive and largest in the vicinity of the q_x-q_y coordinates where the minima in the elastic patterns appear. This reflects that a transition induced by an inelastically scattered x-ray photon is more likely to occur from the $B\,^1\Sigma_u^+$ state than from the $X\,^1\Sigma_g^+$ ground state. Like the elastic patterns, the inelastic ones are centrosymmetric and obey Friedel's law. Two symmetric maxima on the q_x axis dominate the patterns. At $\tau = T_{vib}$ and $q_x \approx \pm 0.87$ Å^{-1}, these maxima are roughly 0.17. At $\tau = (1/2)\,T_{vib}$ and $\tau = (3/2)\,T_{vib}$, the maxima increase to approximately 0.21 and move closer to the origin to $q_x \approx \pm 0.64$ Å^{-1}. As before, these changes are caused by the nuclear motion.

The fact that the inelastic component in Fig. 3 is calculated by subtraction of the elastic from the total signal, not by solving the sum-over-states expression Eq. (20), implies that it is intrinsically converged. In contrast to our previous work (*see Ref.* 28), it is therefore possible to quantify the magnitude of the inelastic component and to compare it to the elastic signal. Remarkably, the inelastic difference scattering is on the same order of magnitude as the elastic. Its maxima amount to more than 60% of the absolute minimum values of the corresponding elastic patterns. This demonstrates clearly that the inelastic component contributes significantly to the total difference scattering and cannot be neglected.

Finally, the total difference scattering patterns are shown in the bottom row of Fig. 3. They are predominantly negative with only small positive signal at large values of q and at angles around 0° or 180°. Naturally, the patterns display the same D_2 rosette group symmetry as their elastic and inelas-

tic components. Again, two symmetric minima on the q_x axis dominate. At $\tau = T_{\mathrm{vib}}$ and $q_x \approx \pm 1.05$ Å^{-1}, they are roughly -0.09. At $\tau = (1/2)\ T_{\mathrm{vib}}$ and $\tau = (3/2)\ T_{\mathrm{vib}}$, the minima decrease to approximately -0.14 and move closer to the origin to $q_x \approx \pm 0.80$ Å^{-1}. Due to the opposite signs of the elastic and inelastic components and their comparable magnitudes, the intensity of the total difference scattering is significantly weaker than the pure elastic signal. The minima appear to be only around 35% to 42% as strong. However, the contrast between the patterns at the inner and outer turning points is more pronounced in the total scattering. The positions of the minima are furthermore shifted by 0.12 Å^{-1} towards larger values of q relative to the elastic signal. This shift is roughly half as large as the shift that is caused by the nuclear dynamics. These differences demonstrate again that the inelastic scattering adds to the time-dependent changes of the elastic component and has to be considered.

In contrast to the case discussed in our previous work (*see Ref.* 28), the total difference scattering patterns in Fig. 3 do not display additional signatures of the coherent mixed component given by Eq. (31). As already stated before, the large detection window and the pulse duration of $d_{\mathrm{x}} = 10$ fs preclude a detection of the coherent mixed signal. Due to the relatively large separation of the potential energy curves of the $\mathrm{X}^1\Sigma_{\mathrm{g}}^+$ and $\mathrm{B}^1\Sigma_{\mathrm{u}}^+$ states, the coherent mixed component oscillates rapidly with a period of roughly 300 as and a subfemtosecond pulse would be required for its detection. Moreover, the coherent mixed component vanishes in the limit of the large detection window defined by Eq. (22) because of the different inversion symmetries of the two states.

C. Comment on the Independent Atom Model

With respect to the widely adapted IAM[72,73], we note that the model cannot provide a good approximation to the scattering patterns presented in Fig. 3. It neither accounts for the redistribution of the one-electron density as a result of the excitation, which strongly affects the elastic component, nor for any of the changes in the inelastic component.[29] Though the severity of the model's failure is aggravated by the fact that the hydrogen molecule has only two electrons and the IAM can be expected to perform better when heavier elements are involved, applications to excited molecules in the gas phase should be met with caution. The IAM proved to approximate the absolute scattering signal of stationary molecules reasonably well, but it is not guaranteed that the same holds for time-dependent difference scattering signals. Even if the effect of an electronic transition or alterations of the inelastic component are small in terms of the absolute intensity, they may contribute significantly to the changes isolated in the difference scattering signal. This can perhaps be understood in analogy to the role of electron correlation in quantum chemistry: it amounts only to a small fraction of the total electronic energy, but strongly affects the energy differences that are measured in spectroscopy or in the dynamics of chemical reactions.

IV. SUMMARY AND CONCLUSION

To summarize, we present a theoretical description of ultrafast time-resolved x-ray scattering by molecules in the gas phase based on first-order time-dependent perturbation theory and quantum electrodynamics. We have recast existing theory[39,40] into a coherent and unified framework and explained several details and implications that were not yet fully discussed in published literature. The effect of the detection window is analyzed in detail and different contributions to the scattering signal are identified. For intermediate detection windows that do not allow for discrimination between different rovibrational transitions, this consists of the elastic, the electronically inelastic, and the coherent mixed components. For larger detection windows that do not distinguish between electronic transitions, the total x-ray scattering signal is split into a one-electron, two-electron, and coherent mixed component. We show that the one-electron component yields a constant, global background, whereas all temporal and structural information is contained in the two-electron component, *i.e.* the excess scattering of Waller and Hartree[48]. Since the latter is related to the Fourier transform of the two-electron density, we emphasize that time-resolved total x-ray scattering by molecules in the gas phase probes more than just the one-electron density and thus provides information beyond the molecular structure. This is in marked contrast to diffraction by crystalline matter, which measures predominantly the Fourier transform of the one-electron density due to coherent amplification of its elastic component.

The coherent mixed scattering is explained in the limit of both intermediate and large detection windows and the conditions necessary for its detection are specified. This further elaborates the theoretical basis for our recent article on the role of electronic coherence in time-resolved x-ray scattering by molecules.[28] It is worth mentioning that the coherent mixed component is caused by intramolecular interference of scattering amplitudes from different electronic states coherently occupied by the molecular wave packet, and should not be confused with the heterodyne interferences that were rejected in a recent debate.[37,43–45] Those erroneous heterodyne terms were ascribed to interference between different elastic scattering amplitudes or atomic form factors in an incoherent superposition of states. The coherent mixed component discussed herein always involves at least one electronically inelastic scattering amplitude and can only be detected if the molecule displays some degree of electronic coherence. An incoherent superposition of states in a gas phase sample will inevitably lead to a scattering signal that is purely elastic and inelastic. The detection of heterodyne effects in x-ray scattering is possible only in diffraction by crystalline matter where elastic scattering amplitudes of different atoms can interfere periodically.[43]

We show simulations of two-dimensional time-resolved total scattering patterns from a hydrogen molecule excited from the $\mathrm{X}^1\Sigma_{\mathrm{g}}^+(v=0)$ ground state to the $\mathrm{B}^1\Sigma_{\mathrm{u}}^+$ first excited state. Both the elastic and the inelastic components are found to display strong signatures of the nuclear motion as well as of the excitation to the $\mathrm{B}^1\Sigma_{\mathrm{u}}^+$ state. These signatures point towards

the shortcomings of the widely adapted Independent Atom Model, as discussed in Subsection III C.

Moreover, the coherent mixed component vanished as a consequence of the limit of a large detection window and the chosen x-ray pulse duration of $d_x = 10$ fs (FWHM). The total scattering signal thus reduced to its elastic and inelastic or one- and two-electron components, respectively. Note that this contrasts with our preceding study (*see Ref.* 28) where the assumed limit of an intermediate detection window and the subfemtosecond pulse duration of $d_x = 100$ as (FWHM) allowed for a detection of the coherent mixed component. An obvious continuation of the present work is to examine the elastic, inelastic, and coherent mixed contributions in polyatomic molecules.

We also note that ultrafast electron diffraction is a closely related experimental technique, both in terms of observables[74,75] and the physical nature of the scattering process.[56,76] Unsurprisingly, for sufficiently coherent electron beams, directly analogous effects to the coherent mixed component described in the current paper appear.[77,78]

The theory presented in this paper provides a conceptual framework that can be used to analyze existing and future time-resolved non-resonant x-ray scattering experiments. The framework is well aligned with the formalism required to simulate photochemical and photophysical processes in molecules in the gas-phase. In the condensed phase, a density matrix formalism might potentially be useful to include relaxation processes[25,37]. Theory will indisputably aid the development of novel experiments to exploit the vast potential of XFELs for ultrafast science. This requires continued theoretical investigation, advanced numerical simulations, and close collaboration between theoreticians and experimentalists to identify challenges on both sides.

ACKNOWLEDGMENTS

A.K. acknowledges support from a Royal Society of Edinburgh Sabbatical Fellowship (58507) and, with A.M.C., a research grant from the Carnegie Trust for the Universities of Scotland (CRG050414). M.S. acknowledges support from HPC-EUROPA3 (INFRAIA-2016-1-730897). The computational work reported used the ARCHER UK National Supercomputing Service (http://www.archer.ac.uk) and support from the Edinburgh Parallel Computing Center (EPCC) is acknowledged.

[1]The Nobel Prize in Physics was awarded to Max von Laue in 1914 "*for his discovery of the diffraction of x-rays by crystals*"[?] and to William and Lawrence Bragg in 1915 "*for their services in the analysis of crystal structure by means of x-rays*"[?] .

[2]P. Emma, R. Akre, J. Arthur, R. Bionta, C. Bostedt, J. Bozek, A. Brachmann, P. Bucksbaum, R. Coffee, F.-J. Decker, Y. Ding, D. Dowell, S. Edstrom, A. Fisher, J. Frisch, S. Gilevich, J. Hastings, G. Hays, P. Hering, Z. Huang, R. Iverson, H. Loos, M. Messerschmidt, A. Miahnahri, S. Moeller, H.-D. Nuhn, G. Pile, D. Ratner, J. Rzepiela, D. Schultz, T. Smith, P. Stefan, H. Tompkins, J. Turner, J. Welch, W. White, J. Wu, G. Yocky, and J. Galayda, "First lasing and operation of an ångstrom-wavelength free-electron laser," Nat. Photon. **4**, 641–647 (2010).

[3]T. Ishikawa, H. Aoyagi, T. Asaka, Y. Asano, N. Azumi, T. Bizen, H. Ego, K. Fukami, T. Fukui, Y. Furukawa, S. Goto, H. Hanaki, T. Hara, T. Hasegawa, T. Hatsui, A. Higashiya, T. Hirono, N. Hosoda, M. Ishii, T. Inagaki, Y. Inubushi, T. Itoga, Y. Joti, M. Kago, T. Kameshima, H. Kimura, Y. Kirihara, A. Kiyomichi, T. Kobayashi, C. Kondo, T. Kudo, H. Maesaka, X. M. Maréchal, T. Masuda, S. Matsubara, T. Matsumoto, T. Matsushita, S. Matsui, M. Nagasono, N. Nariyama, H. Ohashi, T. Ohata, T. Ohshima, S. Ono, Y. Otake, C. Saji, T. Sakurai, T. Sato, K. Sawada, T. Seike, K. Shirasawa, T. Sugimoto, S. Suzuki, S. Takahashi, H. Takebe, K. Takeshita, K. Tamasaku, H. Tanaka, R. Tanaka, T. Tanaka, T. Togashi, K. Togawa, A. Tokuhisa, H. Tomizawa, K. Tono, S. Wu, M. Yabashi, M. Yamaga, A. Yamashita, K. Yanagida, C. Zhang, T. Shintake, H. Kitamura, and N. Kumagai, "A compact x-ray free-electron laser emitting in the sub-ångström region," Nat. Photon. **6**, 540–544 (2012).

[4]European XFEL, "Facts and Figures," (2018), Retrieved 24 July.

[5]Paul Scherrer Institut, "SwissFEL Accelerator," (2018), Retrieved 24 July.

[6]D. Arnlund, L. C. Johansson, C. Wickstrand, A. Barty, G. J. Williams, E. Malmerberg, J. Davidsson, D. Milathianaki, D. P. DePonte, R. L. Shoeman, D. Wang, D. James, G. Katona, S. Westenhoff, T. A. White, A. Aquila, S. Bari, P. Berntsen, M. Bogan, T. B. van Driel, R. B. Doak, K. S. Kjær, M. Frank, R. Fromme, I. Grotjohann, R. Henning, M. S. Hunter, R. A. Kirian, I. Kosheleva, C. Kupitz, M. Liang, A. V. Martin, M. M. Nielsen, M. Messerschmidt, M. M. Seibert, J. Sjöhamn, F. Stellato, U. Weierstall, N. A. Zatsepin, J. C. H. Spence, P. Fromme, I. Schlichting, S. Boutet, G. Groenhof, H. N. Chapman, and R. Neutze, "Visualizing a protein quake with time-resolved x-ray scattering at a free-electron laser," Nat. Methods **11**, 923–926 (2014).

[7]M. P. Minitti, J. M. Budarz, A. Kirrander, J. Robinson, T. J. Lane, D. Ratner, K. Saita, T. Northey, B. Stankus, V. Cofer-Shabica, J. Hastings, and P. M. Weber, "Toward structural femtosecond chemical dynamics: imaging chemistry in space and time," Faraday Discuss. **171**, 81–91 (2014).

[8]M. P. Minitti, J. M. Budarz, A. Kirrander, J. S. Robinson, D. Ratner, T. J. Lane, D. Zhu, J. M. Glownia, M. Kozina, H. T. Lemke, M. Sikorski, Y. Feng, S. Nelson, K. Saita, B. Stankus, T. Northey, J. B. Hastings, and P. M. Weber, "Imaging molecular motion: Femtosecond x-ray scattering of an electrocyclic chemical reaction," Phys. Rev. Lett. **114**, 255501 (2015).

[9]K. H. Kim, J. G. Kim, S. Nozawa, T. Sato, K. Y. Oang, T. W. Kim, H. Ki, J. Jo, S. Park, C. Song, T. Sato, K. Ogawa, T. Togashi, K. Tono, M. Yabashi, T. Ishikawa, J. Kim, R. Ryoo, J. Kim, H. Ihee, and S.-I. Adachi, "Direct observation of bond formation in solution with femtosecond x-ray scattering," Nature **518**, 385–389 (2015).

[10]M. Levantino, G. Schiró, H. T. Lemke, C. Grazia, J. M. Glownia, Z. Diling, M. Chollet, H. Ihee, and A. C. amd M. Cammarata, "Ultrafast myoglobin structural dynamics observed with an x-ray free-electron laser," Nat. Commun. **6**, 6772 (2015).

[11]J. G. Kim, T. W. Kim, J. Kim, and H. Ihee, "Protein structural dynamics revealed by time-resolved x-ray solution scattering," Accounts Chem. Res. **48**, 2200–2208 (2015).

[12]J. M. Budarz, M. P. Minitti, D. V. Cofer-Shabica, B. Stankus, A. Kirrander, J. B. Hastings, and P. M. Weber, "Observation of femtosecond molecular dynamics via pump–probe gas phase x-ray scattering," J. Phys. B: At. Mol. Opt. Phys. **49**, 034001 (2016).

[13]K. Haldrup, W. Gawelda, R. Abela, R. Alonso-Mori, U. Bergmann, A. Bordage, M. Cammarata, S. E. Canton, A. O. Dohn, T. B. van Driel, D. M. Fritz, A. Galler, P. Glatzel, T. Harlang, K. S. Kjær, H. T. Lemke, K. B. Møller, Z. Németh, M. Pápai, N. Sas, J. Uhlig, D. Zhu, G. Vankó, V. Sundström, M. M. Nielsen, and C. Bressler, "Observing solvation dynamics with simultaneous femtosecond x-ray emission spectroscopy and x-ray scattering," J. Phys. Chem. B **120**, 1158–1168 (2016).

[14]E. Biasin, T. B. van Driel, K. S. Kjær, A. O. Dohn, M. Christensen, T. Harlang, P. Chabera, Y. Liu, J. Uhlig, M. Pápai, Z. Németh, R. Hartsock, W. Liang, J. Zhang, R. Alonso-Mori, M. Chollet, J. M. Glownia, S. Nelson, D. Sokaras, T. A. Assefa, A. Britz, A. Galler, W. Gawelda, C. Bressler, K. J. Gaffney, H. T. Lemke, K. B. Møller, M. M. Nielsen, V. Sundström, G. Vankó, K. Wärnmark, S. E. Canton, and K. Haldrup, "Femtosecond x-ray scattering study of ultrafast photoinduced structural dynamics in solvated $[Co(terpy)_2]^{2+}$," Phys. Rev. Lett. **117**, 013002 (2016).

[15]H. Yong, N. Zotev, B. Stankus, J. M. Ruddock, D. Bellshaw, S. Boutet, T. J. Lane, M. Liang, S. Carbajo, J. S. Robinson, W. Du, N. Goff, Y. Chang, J. E. Koglin, M. D. J. Waters, T. I. Sølling, M. P. Minitti, A. Kirrander, and P. M. Weber, "Determining Orientations of Optical Transition Dipole Moments Using Ultrafast X-ray Scattering," J. Phys. Chem. Lett. **9**, 6556–

6562 (2018).
[16]J. M. Ruddock, N. Zotev, B. Stankus, H.-W. Yong, D. Bellshaw, S. Boutet, T. J. Lane, M. Liang, S. Carbajo, W. Du, A. Kirrander, M. P. Minitti, and P. M. Weber, "Simplicity beneath complexity: Counting molecular electronsreveals transients and kinetics of photodissociation reactions," Angew. Chem. Int. Ed. **58**, 6371–6375 (2019).
[17]K. Haldrup, G. Levi, E. Biasin, P. Vester, M. G. Laursen, F. Beyer, K. S. Kjær, T. Brandt van Driel, T. Harlang, A. O. Dohn, R. J. Hartsock, S. Nelson, J. M. Glownia, H. T. Lemke, M. Christensen, K. J. Gaffney, N. E. Henriksen, K. B. Møller, and M. M. Nielsen, "Ultrafast X-Ray Scattering Measurements of Coherent Structural Dynamics on the Ground-State Potential Energy Surface of a Diplatinum Molecule," Phys. Rev. Lett. **122**, 063001 (2019).
[18]B. Stankus, H. Yong, N. Zotev, J. M. Ruddock, D. Bellshaw, T. J. Lane, M. Liang, S. Boutet, S. Carbajo, J. S. Robinson, W. Du, N. Goff, Y. Chang, J. E. Koglin, M. P. Minitti, A. Kirrander, and P. M. Weber, "Ultrafast X-ray scattering reveals vibrational coherence following Rydberg excitation," Nature Chemistry **11**, 716–721 (2019).
[19]C. C. Pemberton, Y. Zhang, K. Saita, A. Kirrander, and P. M. Weber, "From the (1B) Spectroscopic State to the Photochemical Product of the Ultrafast Ring-Opening of 1,3-Cyclohexadiene: A Spectral Observation of the Complete Reaction Path," J. Phys. Chem. A **119**, 8832 (2015).
[20]A. A. Zholents and W. M. Fawley, "Proposal for intense attosecond radiation from an x-ray free-electron laser," Phys. Rev. Lett. **92**, 224801 (2004).
[21]T. Tanaka, "Proposal for a pulse-compression scheme in x-ray free-electron lasers to generate a multiterawatt, attosecond x-ray pulse," Phys. Rev. Lett. **110**, 084801 (2013).
[22]D. J. Dunning, B. W. J. McNeil, and N. R. Thompson, "Few-cycle pulse generation in an x-ray free-electron laser," Phys. Rev. Lett. **110**, 104801 (2013).
[23]E. Prat and S. Reiche, "Simple method to generate terawatt-attosecond x-ray free-electron-laser pulses," Phys. Rev. Lett. **114**, 244801 (2015).
[24]N. Hartmann, G. Hartmann, R. Heider, M. S. Wagner, M. Ilchen, J. Buck, A. O. Lindahl, C. Benko, J. Grünert, J. Krzywinski, J. Liu, A. A. Lutman, A. Marinelli, T. Maxwell, A. A. Miahnahri, S. P. Moeller, M. Planas, J. Robinson, A. K. Kazansky, N. M. Kabachnik, J. Viefhaus, T. Feurer, R. Kienberger, R. N. Coffee, and W. Helml, "Attosecond time–energy structure of X-ray free-electron laser pulses," Nat. Phot. **12**, 215–220 (2018).
[25]J. Cao and K. R. Wilson, "Ultrafast x-ray diffraction theory," J. Phys. Chem. A **102**, 9523–9530 (1998).
[26]U. Lorenz, K. B. Møller, and N. E. Henriksen, "On the interpretation of time-resolved anisotropic diffraction patterns," New J. Phys. **12**, 113022 (2010).
[27]K. B. Møller and N. E. Henriksen, "Time-resolved x-ray diffraction: The dynamics of the chemical bond," Struct. Bond. **142**, 185–212 (2012).
[28]M. Simmermacher, N. E. Henriksen, K. B. Møller, A. M. Carrascosa, and A. Kirrander, "Electronic coherence in ultrafast x-ray scattering from molecular wave packets," Phys. Rev. Lett. **122**, 073003 (2019).
[29]A. M. Carrascosa, H. Yong, D. L. Crittenden, P. M. Weber, and A. Kirrander, "Ab-initio calculation of total x-ray scattering from molecules," J. Chem. Theory Comp. **15**, 2836–2846 (2019), https://doi.org/10.1021/acs.jctc.9b00056.
[30]T. Northey, N. Zotev, and A. Kirrander, "Ab initio calculation of molecular diffraction," J. Chem. Theory Comput. **10**, 4911–4920 (2014).
[31]T. Northey, A. M. Carrascosa, S. Schäfer, and A. Kirrander, "Elastic X-ray scattering from state-selected molecules," J. Chem. Phys. **145**, 154304 (2016).
[32]G. Dixit, O. Vendrell, and R. Santra, "Imaging electronic quantum motion with light," Proc. Natl. Acad. Sci. U.S.A. **109**, 11636–11640 (2012).
[33]M. Ben-Nun, T. J. Martínez, P. M. Weber, and K. R. Wilson, "Direct imaging of excited electronic states using diffraction techniques: theoretical considerations," Chem. Phys. Lett. **262**, 405–414 (1996).
[34]M. Ben-Nun, J. Cao, and K. R. Wilson, "Ultrafast x-ray and electron diffraction: Theoretical considerations," J. Phys. Chem. A **101**, 8743–8761 (1997).
[35]M. Kowalewski, K. Bennett, and S. Mukamel, "Monitoring nonadiabatic avoided crossing dynamics in molecules by ultrafast x-ray diffraction," Struct. Dyn. **4**, 054101 (2017).
[36]M. Simmermacher, N. E. Henriksen, and K. B. Møller, "Time-resolved x-ray scattering by electronic wave packets: analytic solutions to the hydrogen atom," Phys. Chem. Chem. Phys. **19**, 19740–19749 (2017).
[37]K. Bennett, M. Kowalewski, J. R. Rouxel, and S. Mukamel, "Monitoring molecular nonadiabatic dynamics with femtosecond x-ray diffraction," Proc. Natl. Acad. Sci. U.S.A. **115**, 6538–6547 (2018).
[38]S. Bratos, F. Mirloup, R. Vuilleumier, and M. Wulff, "Time-resolved x-ray diffraction: Statistical theory and its application to the photo-physics of molecular iodine," J. Chem. Phys. **116**, 10615–10625 (2002).
[39]N. E. Henriksen and K. B. Møller, "On the theory of time-resolved x-ray diffraction," J. Phys. Chem. B **112**, 558–567 (2008).
[40]U. Lorenz, K. B. Møller, and N. E. Henriksen, "Theory of time-resolved inelastic x-ray diffraction," Phys. Rev. A **81**, 023422 (2010).
[41]A. Kirrander, K. Saita, and D. V. Shalashilin, "Ultrafast X-ray Scattering from Molecules," J. Chem. Theory Comput. **12**, 957–967 (2016).
[42]J. M. Glownia, A. Natan, J. P. Cryan, R. Hartsock, M. Kozina, M. P. Minitti, S. Nelson, J. Robinson, T. Sato, T. van Driel, G. Welch, C. Weninger, D. Zhu, and P. H. Bucksbaum, "Self-referenced coherent diffraction x-ray movie of ångstrom- and femtosecond-scale atomic motion," Phys. Rev. Lett. **117**, 153003 (2016).
[43]K. Bennett, M. Kowalewski, and S. Mukamel, "Comment on "self-referenced coherent diffraction x-ray movie of ångstrom- and femtosecond-scale atomic motion"," Phys. Rev. Lett. **119**, 069301 (2017).
[44]J. M. Glownia, A. Natan, J. P. Cryan, R. Hartsock, M. Kozina, M. P. Minitti, S. Nelson, J. Robinson, T. Sato, T. van Driel, G. Welch, C. Weninger, D. Zhu, and P. H. Bucksbaum, "Glownia et al. reply:," Phys. Rev. Lett. **119**, 069302 (2017).
[45]G. Dixit and R. Santra, "Time-resolved ultrafast x-ray scattering from an incoherent electronic mixture," Phys. Rev. A **96**, 053413 (2017).
[46]Since δ is related to the angular frequencies of the scattered x-ray photons by a Fourier transform of the linear coherence function $C(\delta)$, *see Eq. (12)*, the adiabatic approximation solely affects the energy that is transferred between the molecule and the photons. Eq. (7) is therefore valid as long as the detector is not sensitive to the corresponding changes in photon energy. In experiments in which the non-resonant scattering signal $d\sigma/d\Omega$ does not resolve energy transfer, this condition is usually met. *See also the discussion below Eq. (16).*
[47]T. Helgaker, P. Jørgensen, and J. Olsen, *Molecular Electronic-Structure Theory* (John Wiley & Sons, 2012) pp. 64–66.
[48]I. Waller and D. R. Hartree, "On the intensity of total scattering of x-rays," P. R. Soc. Lond. A **124**, 119–142 (1929).
[49]G. Dixit, J. M. Slowik, and R. Santra, "Theory of time-resolved nonresonant x-ray scattering for imaging ultrafast coherent electron motion," Phys. Rev. A **89**, 043409 (2014).
[50]M. Vacher, M. J. Bearpark, M. A. Robb, and J. P. Malhado, "Electron dynamics upon ionization of polyatomic molecules: Coupling to quantum nuclear motion and decoherence," Phys. Rev. Lett. **118**, 083001 (2017).
[51]C. Arnold, O. Vendrell, and R. Santra, "Electronic decoherence following photoionization: Full quantum-dynamical treatment of the influence of nuclear motion," Phys. Rev. A **95**, 033425 (2017).
[52]A. R. Bainbridge, J. Harrington, A. Kirrander, C. Cacho, E. Springate, W. A. Bryan, and R. S. Minns, "VUV excitation of a vibrational wavepacket in D_2 measured through strong-field dissociative ionization," New J. Phys. **17**, 103013 (2015).
[53]P. J. Knowles and H.-J. Werner, "An efficient second-order mc scf method for long configuration expansions," Chem. Phys. Lett. **115**, 259–267 (1985).
[54]D. E. Woon and T. H. Dunning, "Gaussian basis sets for use in correlated molecular calculations. iv. calculation of static electrical response properties," J. Chem. Phys. **100**, 2975–2988 (1994).
[55]H.-J. Werner, P. J. Knowles, G. Knizia, F. R. Manby, and M. Schütz, "Molpro: a general-purpose quantum chemistry program package," WIREs Comput. Mol. Sci. **2**, 242–253 (2012).
[56]A. M. Carrascosa and A. Kirrander, "Ab initio calculations of inelastic scattering," Phys. Chem. Chem. Phys. **19**, 19545–19553 (2017).
[57]N. Zotev, A. M. Carrascosa, M. Simmermacher, and A. Kirrander, "Excited electronic states in total isotropic scattering from molecules," J. Chem. Theory Comput. (2019), submitted.
[58]J. Wang and V. H. Smith, "Evaluation of cross sections for x-ray and high-energy electron scattering from molecular systems," Int. J. Quantum Chem. **52**, 1145–1151 (1994).
[59]M. D. Feit, J. A. Fleck, and A. Steiger, "Solution of the schrödinger equa-

tion by a spectral method," J. Comput. Phys. **47**, 412–433 (1982).
[60]B. Schmidt and U. Lorenz, "Wavepacket: A matlab package for numerical quantum dynamics. i: Closed quantum systems and discrete variable representations," Comput. Phys. Commun. **213**, 223–234 (2017).
[61]D. Kosloff and R. Kosloff, "A fourier method solution for the time dependent schrödinger equation as a tool in molecular dynamics," J. Comput. Phys. **52**, 35–53 (1983).
[62]L. Wolniewicz, T. Orlikowski, and G. Staszewska, "$^1\sigma_u$ and $^1\pi_u$ states of the hydrogen molecule: Nonadiabatic couplings and vibrational levels," J. Mol. Spectrosc. **238**, 118–126 (2006).
[63]L. Wolniewicz, "Nonadiabatic energies of the ground state of the hydrogen molecule," J. Chem. Phys. **103**, 1792–1799 (1995).
[64]G. Staszewska and L. Wolniewicz, "Adiabatic energies of excited $^1\sigma_u$ states of the hydrogen molecule," J. Mol. Spectrosc. **212**, 208–212 (2002).
[65]L. Wolniewicz and G. Staszewska, "$^1\sigma_u^+ \longrightarrow x^1\sigma_g^+$ transition moments for the hydrogen molecule," J. Mol. Spectrosc. **217**, 181–185 (2003).
[66]H.-J. Werner and P. J. Knowles, "An efficient internally contracted multiconfiguration-reference configuration interaction method," J. Chem. Phys. **89**, 5803–5814 (1988).
[67]P. J. Knowles and H.-J. Werner, "An efficient method for the evaluation of coupling coefficients in configuration interaction calculations," Chem. Phys. Lett. **145**, 514–522 (1988).
[68]P. J. Knowles and H.-J. Werner, "Internally contracted multiconfiguration-reference configuration interaction calculations for excited states," Theor. Chim. Acta **84**, 95–103 (1992).
[69]L. Wolniewicz and K. Dressler, "Adiabatic potential curves and nonadiabatic coupling functions for the first five excited $^1\sigma_g^+$ states of the hydrogen molecule," J. Chem. Phys. **100**, 444–451 (1994).
[70]L. Wolniewicz, "Adiabatic potentials of the lowest $^1\pi_g$ and $^{1,3}\delta_g$ states of the hydrogen molecule," J. Mol. Spectrosc. **169**, 329–340 (1995).
[71]L. Wolniewicz and G. Staszewska, "Excited $^1\pi_u$ states and the $^1\pi_u \longrightarrow x^1\sigma_g$ transition moments of the hydrogen molecule," J. Mol. Spectrosc. **220**, 45–51 (2003).
[72]L. Bewilogua, "Über die streuung von röntgen- und kathodenstrahlen an freien molekülen," Phys. Z. **33**, 688–692 (1932).
[73]E. Prince, ed., *International Tables for Crystallography Volume C: Mathematical, physical and chemical tables*, 2006th ed., ISBN 978-1-4020-1900-5 (Wiley, 2006).
[74]M. Stefanou, K. Saita, D. V. Shalashilin, and A. Kirrander, "Comparison of ultrafast electron and x-ray diffraction – a computational study," Chem. Phys. Lett. **683**, 300–305 (2017).
[75]T. J. A. Wolf, D. M. Sanchez, J. Yang, R. M. Parrish, J. P. F. Nunes, M. Centurion, R. Coffee, J. P. Cryan, M. Gühr, K. Hegazy, A. Kirrander, R. K. Li, J. Ruddock, X. Shen, T. Veccione, S. P. Weathersby, P. M. Weber, K. Wilkin, H. Yong, Q. Zheng, X. J. Wang, M. P. Minitti, and T. J. Martínez, "Imaging the photochemical ring-opening of 1,3-cyclohexadiene by ultrafast electron diffraction," Nat. Chem. (2019), 10.1038/s41557-019-0252-7.
[76]M. Inokuti, "Inelastic collisions of fast charged particles with atoms and molecules—the bethe theory revisited," Rev. Mod. Phys. **43**, 297–347 (1971).
[77]H.-C. Shao and A. F. Starace, "Imaging Coherent Electronic Motion in Atoms by Ultrafast Electron Diffraction," Phys. Rev. A **88**, 062711 (2013).
[78]H.-C. Shao and A. F. Starace, "Imaging population transfer in atoms with ultrafast electron pulses," Phys. Rev. A **94**, 030702 (2016).

$GK\,^1\Sigma_g^+$
$I\,^1\Pi_g$
$B\,^1\Sigma_u^+$
$B'\,^1\Sigma_u^+$
$EF\,^1\Sigma_g^+$
$C\,^1\Pi_u$
$X\,^1\Sigma_g^+$
15
10
5
0
V (eV)
1
2
3
4
5
6
R (Å)

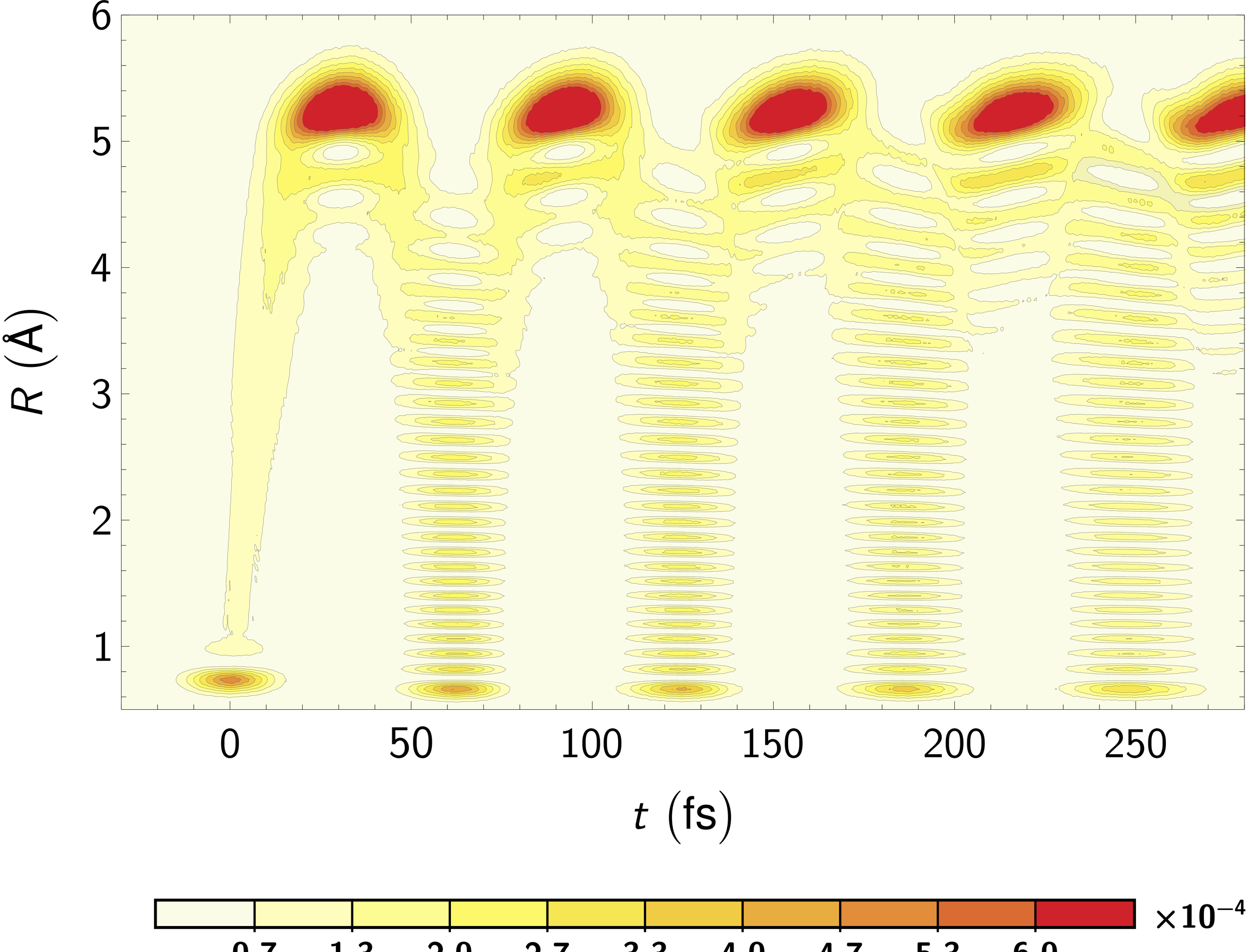
6
5
4
3
2
1
R (Å)
0
50
100
150
200
250
t (fs)
0.7
1.3
2.0
2.7
3.3
4.0
4.7
5.3
6.0
×10−4

$\tau = \frac{1}{2}\,T_{\mathrm{vib}}$ $\tau = T_{\mathrm{vib}}$ $\tau = \frac{3}{2}\,T_{\mathrm{vib}}$

90° 180° 0° 270°

$\times 10^{-1}$

−2.70 −2.10 −1.50 −0.90 −0.30

90° 180° 0° 270°

$\times 10^{-1}$

0.20 0.60 1.00 1.40 1.80

90° 180° 0° 270°

−1.26 −0.84 −0.42 0.00 0.42 0.84 1.26 $\times 10^{-1}$